

## Experimental measurements of telecentricity errors in high-numerical-aperture extreme ultraviolet mask images

Sudharshanan Raghunathan, Obert R. Wood II, Pawitter Mangat, Erik Verduijn, Vicky Philipson, Eric Hendrickx, Rik Jonckheere, Kenneth A. Goldberg, Markus P. Benk, Patrick Kearney, Zachary Levinson, and Bruce W. Smith

Citation: *Journal of Vacuum Science & Technology B* **32**, 06F801 (2014); doi: 10.1116/1.4901876

View online: <http://dx.doi.org/10.1116/1.4901876>

View Table of Contents: <http://scitation.aip.org/content/avs/journal/jvstb/32/6?ver=pdfcov>

Published by the AVS: Science & Technology of Materials, Interfaces, and Processing

### Articles you may be interested in

[Actinic mask metrology for extreme ultraviolet lithography](#)

*J. Vac. Sci. Technol. B* **22**, 264 (2004); 10.1116/1.1643057

[Characterization of extreme ultraviolet lithography mask defects by actinic inspection with broadband extreme ultraviolet illumination](#)

*J. Vac. Sci. Technol. B* **20**, 3000 (2002); 10.1116/1.1523397

[High sensitivity actinic detection of native defects on extreme ultraviolet lithography mask blanks](#)

*J. Vac. Sci. Technol. B* **19**, 2401 (2001); 10.1116/1.1410088

[Characterization of extreme ultraviolet lithography mask defects from extreme ultraviolet far-field scattering patterns](#)

*J. Vac. Sci. Technol. B* **18**, 2930 (2000); 10.1116/1.1319843

[Extreme ultraviolet holographic microscopy and its application to extreme ultraviolet mask-blank defect characterization](#)

*J. Vac. Sci. Technol. B* **18**, 2935 (2000); 10.1116/1.1314382



## Instruments for Advanced Science

<p>Contact Hiden Analytical for further details:  <b>W</b> <a href="http://www.HidenAnalytical.com">www.HidenAnalytical.com</a>  <b>E</b> <a href="mailto:info@hiden.co.uk">info@hiden.co.uk</a></p> <p><b>CLICK TO VIEW</b> our product catalogue</p>	 <p><b>Gas Analysis</b></p> <ul style="list-style-type: none"> <li>› dynamic measurement of reaction gas streams</li> <li>› catalysis and thermal analysis</li> <li>› molecular beam studies</li> <li>› dissolved species probes</li> <li>› fermentation, environmental and ecological studies</li> </ul>	 <p><b>Surface Science</b></p> <ul style="list-style-type: none"> <li>› UHV TPD</li> <li>› SIMS</li> <li>› end point detection in ion beam etch</li> <li>› elemental imaging - surface mapping</li> </ul>	 <p><b>Plasma Diagnostics</b></p> <ul style="list-style-type: none"> <li>› plasma source characterization</li> <li>› etch and deposition process reaction</li> <li>› kinetic studies</li> <li>› analysis of neutral and radical species</li> </ul>	 <p><b>Vacuum Analysis</b></p> <ul style="list-style-type: none"> <li>› partial pressure measurement and control of process gases</li> <li>› reactive sputter process control</li> <li>› vacuum diagnostics</li> <li>› vacuum coating process monitoring</li> </ul>
--	--	--	--	--

# Experimental measurements of telecentricity errors in high-numerical-aperture extreme ultraviolet mask images

Sudharshanan Raghunathan,<sup>a)</sup> Obert R. Wood II, and Pawitter Mangat  
 GLOBALFOUNDRIES, 400 Stonebreak Rd. Extension, Malta, New York 12020

Erik Verduijn  
 GLOBALFOUNDRIES, Kapeldreef 75, Leuven B-3001, Belgium

Vicky Philipsen, Eric Hendrickx, and Rik Jonckheere  
 Imec vzw, Kapeldreef 75, Leuven B-3001, Belgium

Kenneth A. Goldberg and Markus P. Benk  
 Lawrence Berkeley National Laboratory, Center for X-Ray Optics, Cyclotron Road, Berkeley, California 94720

Patrick Kearney  
 SEMATECH, 257 Fuller Road, Albany, New York 12203

Zachary Levinson and Bruce W. Smith  
 Microsystems Engineering Program, Rochester Institute of Technology, Rochester, New York 14623

(Received 31 July 2014; accepted 4 November 2014; published 19 November 2014)

Nontelecentric illumination in extreme ultraviolet (EUV) lithography leads to pattern shifts through focus called telecentricity errors. As the industry moves toward finer pitch structures and higher numerical apertures (NA) to improve resolution, the effects of telecentricity errors become more significant. These telecentricity errors are dependent on pattern pitch, pattern type, lens aberrations, mask stack, to name a few. In this paper, a novel technique to measure telecentricity errors using EUV mask images from an actinic mask inspection tool, called the SEMATECH High NA Actinic Reticle Review Project (SHARP) is presented. SHARP is SEMATECH's second generation actinic mask imaging tool developed by Lawrence Berkeley National Laboratory. The SHARP can image masks at different numerical aperture settings, even beyond the currently available scanner NA of 0.33 (high-NA EUV) and also has a set of programmable illuminator choices. A tuned multilayer EUV mask blank was fabricated with test structures optimized for imaging on SHARP. The test structures were designed to cover a variety of critical dimensions and pitches. The mask design was fabricated on a tuned multilayer blank optimized for NA > 0.4. The mask was fabricated at Advanced Mask Technology Center and imaged on the SHARP. SHARP images were analyzed in software customized for edge position extraction of features. Pattern shifts through focus were calculated for a variety of pitches under different NA and illumination settings. The results show a monotonic increase in pattern shifts as NA increases. Also, at a given NA, the pattern shift is dependent on pattern pitch. The paper provides a detailed discussion on the experiment setup, analysis of the results and applicability of these results to high volume manufacturing of semiconductor devices using production EUV scanners.  
 © 2014 American Vacuum Society. [<http://dx.doi.org/10.1116/1.4901876>]

## I. INTRODUCTION

Extreme ultraviolet (EUV) lithography extensions are being actively investigated to extend the semiconductor scaling roadmap to sub-30 nm pitch dimensions.<sup>1</sup> Approaches to extend EUV patterning resolution include increasing numerical aperture of the projection optics, various double patterning techniques like self-aligned double patterning using spacers, pitch splitting, and various lithography-etch multi-patterning approaches, improving scanner illumination using source mask optimization.<sup>2</sup> In this paper, extendibility of EUV imaging using a higher numerical aperture projection optic system is investigated, particularly focused on

characterizing mask stack induced pattern shifts through focus due to reflectivity apodization.

EUV masks are Bragg reflectors.<sup>3,4</sup> The mask blank consists of a substrate with a multilayer (ML) coating made of pairs of molybdenum and silicon. The structure of the mask blank is shown in Fig. 1. The period of the multilayer coating,  $d$ , is optimized for maximum reflectivity at wavelength ( $\lambda$ ) and incident angle ( $\theta$ ), according to Bragg's law<sup>5</sup>

$$n\lambda = 2d \sin(\theta), \quad (1)$$

where  $n$  is the order of reflected light. For  $n = 1$  and  $\theta = 6^\circ$ , the optimum  $d$  spacing is 7.044 nm. Typically, EUV masks have 40 multilayer pairs of Mo and Si.<sup>3,4</sup> The absorber stack has a capping layer, typically ruthenium, to protect the multilayer film, an absorber and antireflective layer made up of

<sup>a)</sup>Electronic mail: sudhar.raghunathan@globalfoundries.com

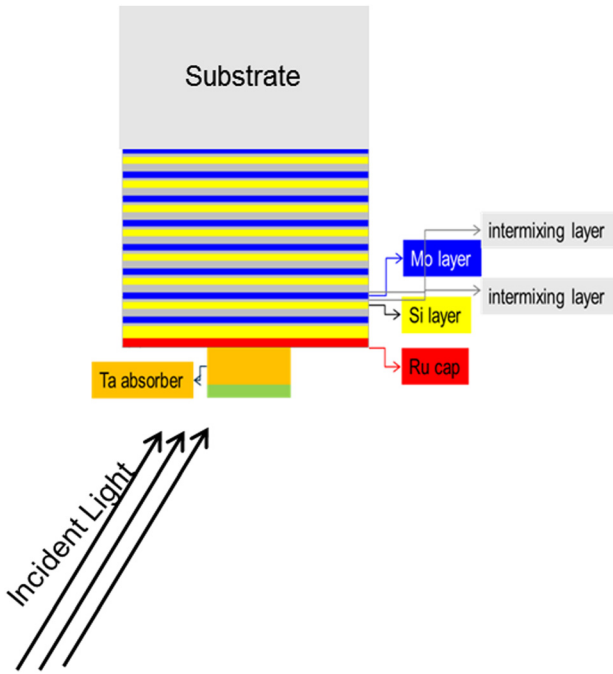


FIG. 1. (Color online) EUV multilayer mask blank with absorber stack, molybdenum and silicon multilayers, and intermixing layers at the interfaces.

TaBN and TaBO, respectively. The thicknesses of these layers vary depending on the mask blank process and patterning requirements. The mask is typically patterned in an electron beam lithography tool with device relevant structures, which opens the absorber regions selectively to reflect light off the multilayer reflector. Figure 2 shows incident and reflected light from a multilayer EUV mask blank. The light is incident on the mask at 6° chief ray angle of incidence (CRAI). The areas where absorber is removed during patterning reflect light. Other areas of the mask absorb incident EUV radiation. Figure 3 shows the change in reflectivity of the mask blank as a function of incidence angle ( $\theta$ ). The reflectivity gradually increases with incidence angles from 0° to ~10°, followed by a significant drop from 10° to ~16°. This change in reflectivity through incidence angle of light

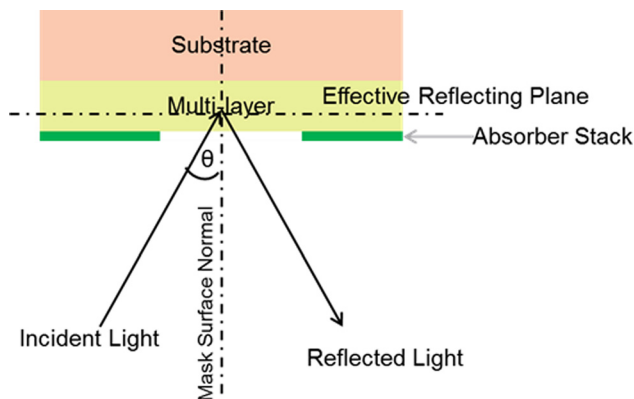


FIG. 2. (Color online) EUV multilayer blank with light incident at 6° CRAI to the mask surface normal.

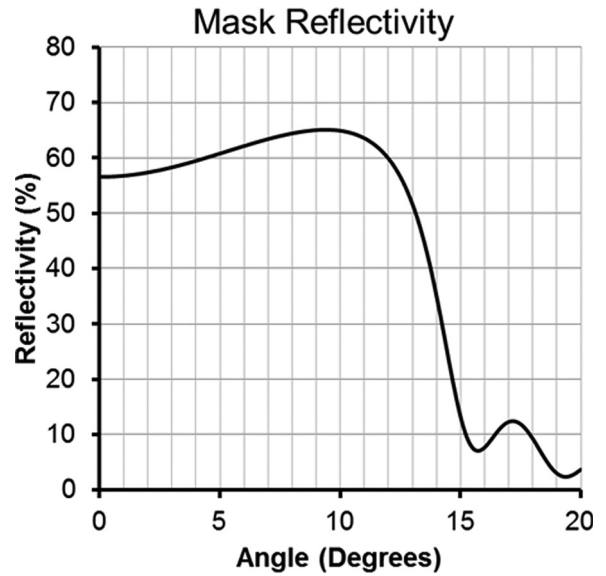


FIG. 3. Change in mask multilayer reflectivity with incident angle on the mask, referred to as mask apodization.

will be referred throughout the remainder of this paper as mask apodization.

Figure 4 shows an illustration of light incident on a EUV mask from a quadrupole illuminator. The poles have 45° openings with inner and outer sigma of 0.7 and 0.9, respectively. The high and low angle incident rays from the source on the multilayer reflector define the maximum and minimum angles in the reflected light. For an NA of 0.25, the range of incident angles around the CRAI can be calculated using

$$\Delta\theta = 2 \times \sin^{-1} \left( \frac{NA}{M} \right), \tag{2}$$

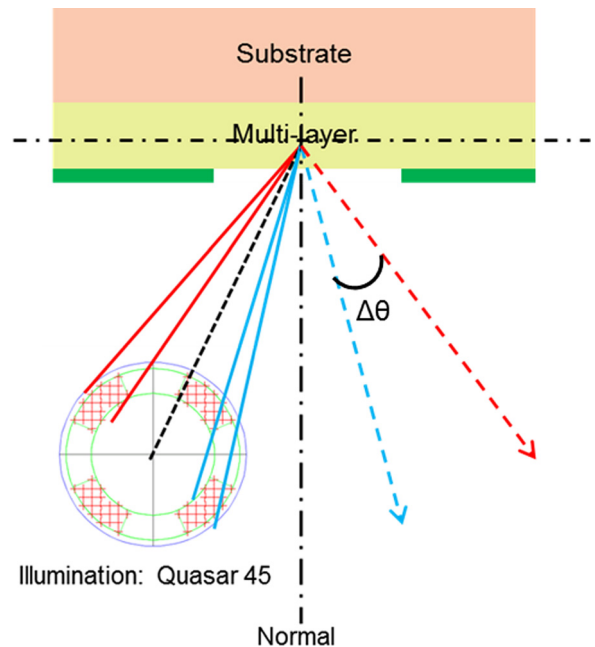


FIG. 4. (Color online) Light incident on the mask in a range of angles around the 6° chief ray angle, for a quadrupole illumination.

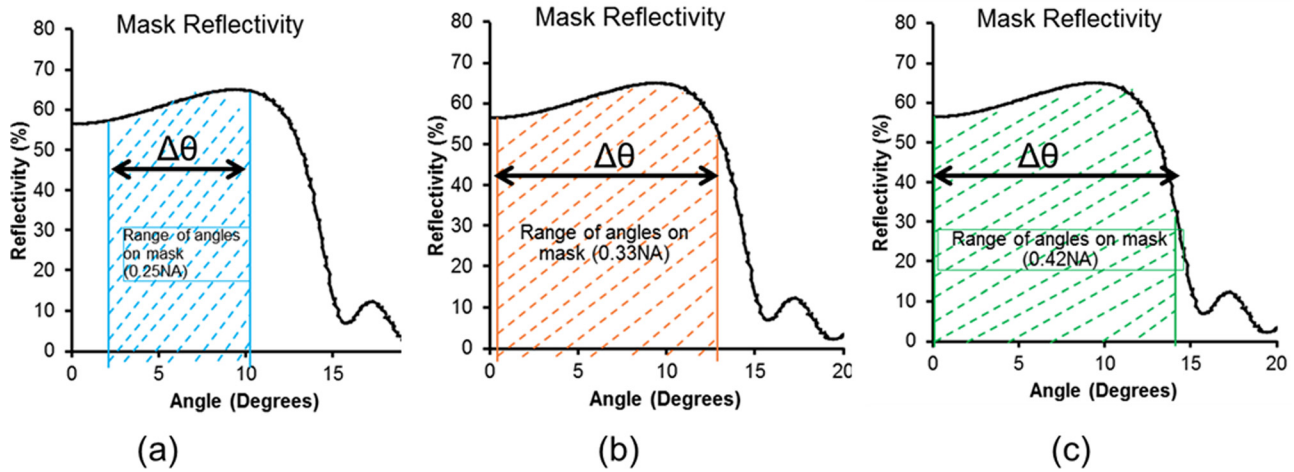


Fig. 5. (Color online) Ranges of angles on the mask multilayer reflectivity apodization curve sampled by (a) 0.25 NA system, (b) 0.33 NA system, and (c) 0.42 NA system. (a) and (b) have a  $6^\circ$  chief-ray-angle, while (c) assumes  $8^\circ$  chief-ray-angle.

where  $M$  is demagnification and  $NA$  is the numerical aperture. Figure 5 shows the range of angles incident on the mask for various projection optics numerical apertures. For a 0.25 NA imaging system, the range is well centered around  $6^\circ$ , with minimal apodization at the lower incidence angles. However, as the NA of the projection optics increases, the range of angles incident on the mask becomes larger. This leads to increased apodization at the larger incidence angles. This increased apodization in turn results in larger 3D mask effects like increased shadow bias, larger pattern shifts through focus and more complicated optical proximity correction requirements.<sup>6-8</sup>

Mask apodization in EUV lithography results in wafer focus error induced pattern shifts. Figure 6 shows multilayer reflectivity change across numerical aperture for a 0.42 NA imaging system due to mask reflectivity apodization. Figure 7(a) shows a dipole illumination used to image a horizontal line space structure. The change in intensity of diffracted light at these poles results in an imbalance in the zeroth and  $\pm 1$ st order. Figure 7(b) shows aerial image intensity across the line space structure through wafer focus. The x-axis is position along the line space pattern and the y-axis is the

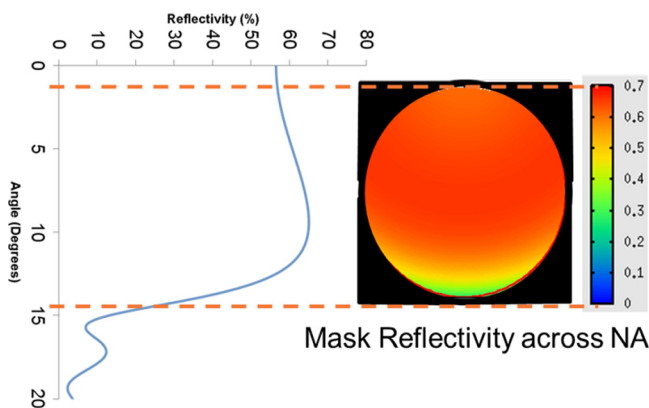


Fig. 6. (Color online) Reflectivity variation across NA due to mask multilayer reflectivity apodization for a 0.42 NA system.

wafer focus error. The intensity scale corresponds to light intensity on wafer. A low intensity in the cross section corresponds to absorber on mask or resist line on wafer. From Fig. 7(b), it can be seen that the size of this low intensity area, i.e., the resist line width, changes as we go through focus. In addition, it is also evident that the position of the center of the resist line changes as we go through focus as well. This change in center position through focus can be captured in a metric called telecentricity error (mrad) given by

$$\text{Telecentricity Error} = \frac{\text{Pattern Shift}}{\text{Focus Range}}. \quad (3)$$

For a focus error of 100 nm, a 20 mrad of telecentricity error means 2 nm of pattern shift through focus. This pattern shift is a significant contributor to technology overlay budgets. A large telecentricity error, leading to large pattern shifts would serve to drive lithography tool focus control budgets on account of meeting overlay budget requirements. Telecentricity error interlinks focus and overlay budgets in EUV lithography. These telecentricity errors can be partly compensated by changing the reflectivity apodization curve for multilayer EUV masks. The mask reflectivity can be changed by tuning the ML factor of the mask blank, where the ML factor is defined as

$$\text{ML Factor} = \frac{d_{\text{tuned}}}{d_{\text{nominal}}}, \quad (4)$$

where  $d_{\text{nominal}}$  is the multilayer period of a EUV blank optimized for 0.25 NA imaging at  $\lambda = 13.5$  nm and CRAI =  $6^\circ$ .

Figure 8 compares the simulated mask apodization curve for a standard multilayer blank with a ML factor of 1 and a tuned blank with a ML factor of 1.014. In both cases, a calibrated mask stack model including silicide intermixing layer between the Mo/Si and Si/Mo interface is used.<sup>9</sup> The range of angles incident on the mask for a projection optics system with 0.42 NA,  $4\times$  demagnification and CRAI  $8^\circ$  are also shown. The standard ML blank has a large drop in

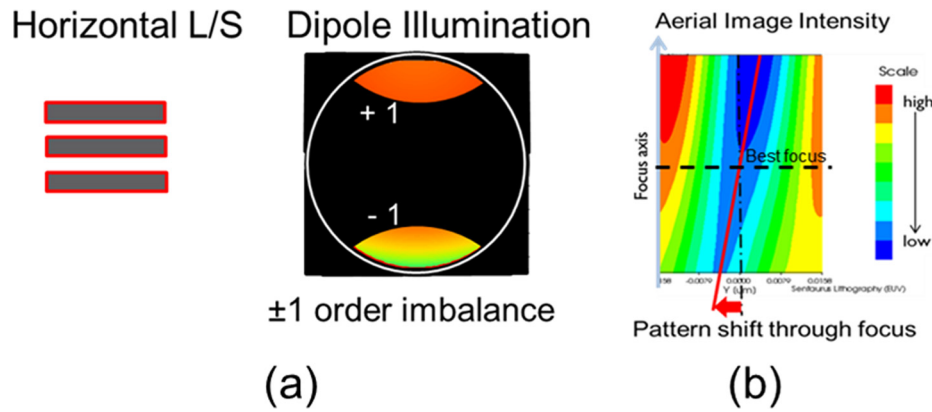


Fig. 7. (Color online) (a) Effect of mask apodization on the intensity of the zeroth and first order light for a dipole Y illumination imaging a horizontal line space grating at the resolution limit. (b) Aerial image intensity cross section of the line space structure showing pattern shift resulting from mask apodization as a function of focus error at the object plane (wafer).

reflectivity at large incidence angles while the tuned ML blank improved reflectivity at large angles while having reduced reflectivity at the smaller angles. Figure 9 is a plot of simulated telecentricity error for a range of pitches at different NA settings for both standard and tuned multilayer blanks using annular illumination with inner and outer sigma of 0.2 and 0.9, respectively, at 0.42 NA. For standard ML blanks, as NA gets larger, the amount of telecentricity errors gets larger. Also, within a given NA, telecentricity errors change depending on pattern pitch. Figure 9(b) shows the improvement in telecentricity errors using a tuned multilayer blank. Tuning the ML factor balances reflectivity for zero and first order light for a particular pitch. A 1.014 ML factor mask blank is optimized for critical pitch ( $\sim 32$  nm) printing at 0.42 NA using  $4\times$  demagnification and CRAI  $8^\circ$ . As seen in the figure, the pitches 24, 32, and 36 nm at 0.42 NA exhibit almost no telecentricity errors. Hence, pattern shift has been minimized at the tightest pitches where the overlay budgets are most critical. This type of multilayer tuning can be effective in minimizing telecentricity errors at a particular range of pitches in EUV lithography.

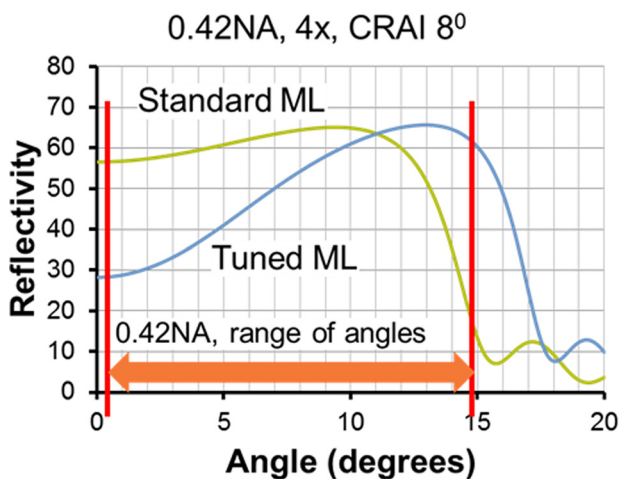


Fig. 8. (Color online) Simulated mask reflectivity apodization curves for a mask blanks with multilayer factor of 1 and 1.014.

## II. EXPERIMENT SETUP

In order to measure the focus induced pattern shifts experimentally, a special multilayer mask blank was fabricated at the SEMATECH Mask Blank Development Center in Albany, NY. Determination of the ML factor was based on minimum telecentricity errors for at-resolution printing at 0.42 NA,  $4\times$  demagnification, and CRAI  $8^\circ$ . The mask blank was patterned at the Advanced Mask Technology Center in Dresden, Germany, with specially designed test structures optimized for extracting pattern shift information. The patterned mask was imaged on the SEMATECH High NA Actinic Reticle Review Project (SHARP) EUV microscope.<sup>10</sup> The images from SHARP were analyzed in a custom image processing software called ThroughFocus from Kanayama Consulting to extract telecentricity errors.

### A. SHARP description

SHARP is a second-generation reticle imaging tool jointly developed by SEMATECH and Lawrence Berkeley National Laboratory (LBNL). The system uses a synchrotron bending-magnet source at LBNL's Advanced Light Source. The illumination is tuned to 13.5-nm wavelength with a bandwidth of  $\lambda/\Delta\lambda = 1450$ , and a customizable pupil fill pattern, achieved using a rapidly scanning mirror in a Fourier-synthesis illuminator. SHARP's illuminator can create disk, annular, dipole, quadrupole, cross-pole, and other custom illumination patterns.<sup>10</sup> The imaging NA is determined by the selection of zone plate lenses. The zone plates are fabricated using electron-beam lithography. The system has customizable  $4\times$  NA values of 0.25, 0.33, 0.35, 0.45, 0.5, and 0.625 depending on the zone plate used for imaging. For the purpose of our study, we limited our experiments to annular illumination with an inner/outer sigma setting of 0.2/0.9. SHARP is capable of navigating the entire active area of the mask and records approximately eight through-focus series per hour. The imaging NA, illumination CRAI and azimuthal angles are designed to mimic production EUV lithography systems. However, SHARP uses a single diffractive optical element to form a magnified image on a CCD sensor.

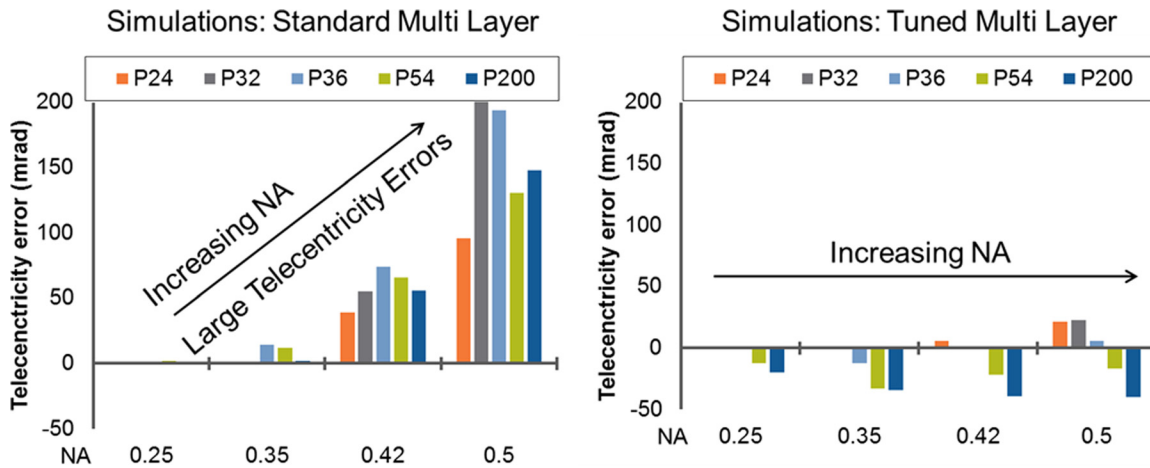


FIG. 9. (Color online) (a) Simulation results showing telecentricity errors increasing through NA using annular illumination (sigma setting 0.2/0.9) for a standard multilayer stack. (b) Simulation results for a 1.014 multilayer factor blank showing telecentricity errors can be compensated for the tightest pitches by changing the mask multilayer factor.

This is in contrast to the demagnifying catoptric lens of an EUV lithography system. Hence, the results from experiments performed on the SHARP require careful consideration to extend learning to production EUV scanners. For example, estimation of SHARP tool artifacts such as zone plate aberrations and illumination nonuniformity is required.

## B. Measurement setup

In order to measure pattern shifts, a suitable set of reference structures is needed. Absolute pattern shifts of a line space grating structure, for example, is very difficult to measure because of the absence of a reference position to measure from. For this purpose, a special test structure was designed that consists of two adjacent gratings: one at target pitch and the other with a larger pitch, serving as a reference. The reference grating pitch is chosen as a multiple of the target pitch. Figure 10 shows the measurement setup. As the test structures are imaged through focus, a relative misalignment between the reference and target pitch grating is observed. This is due to the pitch dependence of the telecentricity error at the given NA and illumination. If the target pitch grating is close to resolution limit and the reference grating is at a relaxed pitch, there is a large relative displacement through focus between the two pitches. The relative

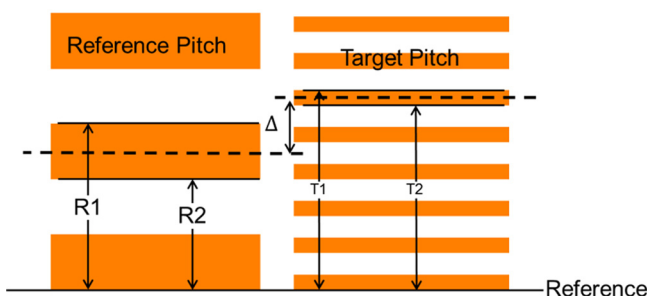


FIG. 10. (Color online) Measurement setup for telecentricity error extraction using a special test structure with target and reference pitch gratings. Relative telecentricity errors are measured as a change in centroid of the target and reference pitch grating through focus.

pattern displacement may be calculated by extracting the edge positions R1 and R2 of the reference grating line and T1 and T2 of the target grating line. Using these edge positions, the centroid of the reference and the target pitch structures are calculated as an average of R1, R2, and T1, T2, respectively. The relative shift is then given as

$$\Delta = \frac{T1 + T2}{2} - \frac{R1 + R2}{2}.$$

Typically, as we image a grating structure through focus, the critical dimension (CD), i.e., width of the line, changes away from nominal focus. The use of centers of the two lines removes the effect of change in CD of these structures through focus. Table I lists the target and reference pitch gratings used in this study. Figure 11 is an example of a through-focus image series of a 36 nm target pitch line and 180 nm reference pitch line, imaged at 0.25 NA using annular illumination.

## III. RESULTS AND DISCUSSION

Figure 12 shows the first experimental measurements of focus-induced pattern shifts in high NA EUV systems measured on the SHARP tool in LBNL. All measurements were made with annular illumination using sigma settings 0.2/0.9. Figures 12(a)–12(d) show measurements made with 0.5, 0.42, 0.35, and 0.25 NA zone plates on the SHARP. The

TABLE I. List of target and reference pitches for the targets imaged on the SHARP.

Target pitch (nm)	Reference pitch (nm)
54	162
50	150
48	144
44	220
40	200
36	180
32	160

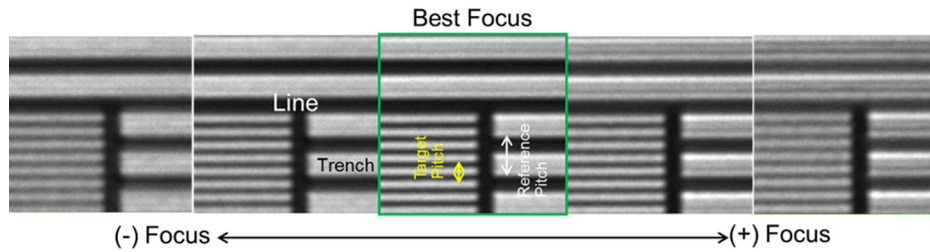


Fig. 11. (Color online) Example of a through focus image series captures on the SHARP tool of a 36 nm target pitch vs a 180 nm reference pitch imaged at NA0.25 using annular illumination.

measurements show that the relative shifts between target and reference pitch gratings become larger as the NA of the system increases. The relative shifts for 0.25 NA over a 200 nm focus range is  $\sim 3$  nm, while the relative shift for 0.5 NA over a 150 nm focus range is 14 nm. Within a given NA, the largest relative shifts tend to occur for the tightest pitch target gratings. Pitch dependence gets larger away from nominal focus. For all NA's, the pattern shifts change from negative to positive values as defocus changes from negative to positive. Since these values are relative, it is important to distinguish whether the target pitch or the reference pitch gratings contribute to these pattern shifts.

### A. Comparison to simulations

Figure 13 is a comparison of relative pattern shift between measured high NA data on the SHARP tool and rigorous 3D mask simulations done in SLITHO<sup>TM</sup> for EUV (Synopsys) for 0.35, 0.42, and 0.5 NA imaging of pitch = 36 nm (P36) and pitch = 180 nm (P180) structures. The simulations use a calibrated mask stack model.<sup>9</sup> The values plotted in the figure are relative shifts between P36 and P180. As seen from the figure, there is an excellent agreement between simulations and measured data for 0.35 and 0.42 NA and good agreement for the 0.5 NA results.

This agreement between simulation and experimental data validates the simulations setup for further understanding the contributions to the relative pattern shift. Figure 14 shows simulation data for individual contributions from P36 and P180 for 0.35, 0.42, and 0.5 NA systems. The pattern shift in the P36 structure is quite large for 0.35 NA, is very small for 0.42 NA and is large again at 0.5 NA. It is also evident that the slope of the pattern shift changes as we move from 0.35 to 0.5 NA. The pattern shift in the P180 structure is large and does not vary much from 0.35 to 0.5 NA. The slope of the pattern shifts is similar for P36 and P180 at 0.35 NA, and is opposite at 0.5 NA. The relative shifts as a result are small at 0.35 NA and large at 0.5 NA, even though the smallest shift for P36 structure occurs at 0.42 NA.

The observations in Sec. II can be explained with the help of pupil maps showing the intensity of the diffracted orders at the various NA and pitches. The pupil maps are shown in Figs. 15(a)–15(c) for 0.35, 0.42, and 0.5 NA systems. The first pair of pupil maps in Fig. 15 show P36 and P180 both have diffracted order imbalance seen as intensity difference between the top and bottom half of the pupil maps. There is a smaller intensity of light going through the top half of the pupil than the bottom half. This results in similar slopes for the pattern shift curves for both P36 and P180. In Fig. 15(b), this imbalance is much smaller at 0.42 NA for P36, while

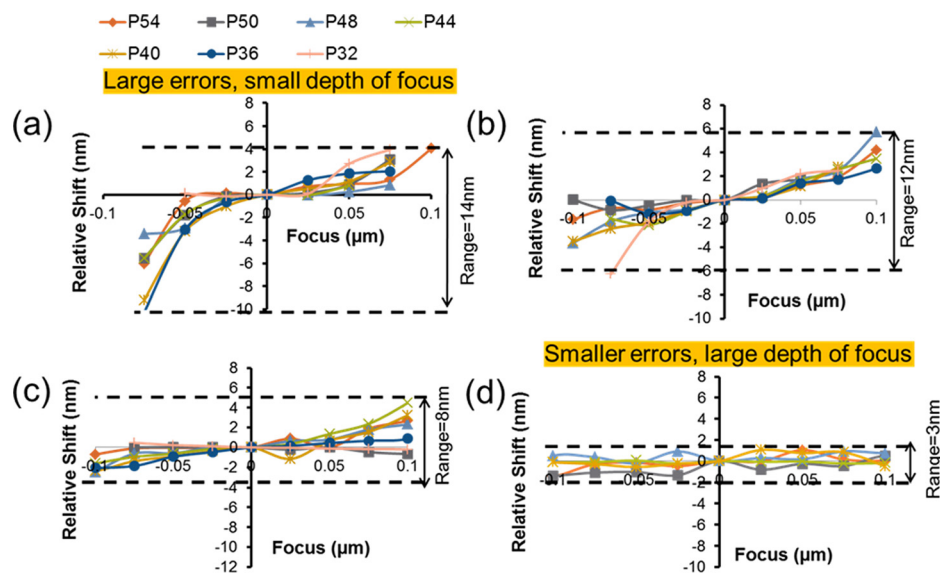


Fig. 12. (Color online) First experimental results showing relative pattern shift from telecentricity errors for NA = 0.25, 0.35, 0.42, and 0.5 for a 0.2/0.9 sigma annular illuminator. Data show relative pattern shifts for target pitches P54, P50, P48, P44, P40, P36, and P32.

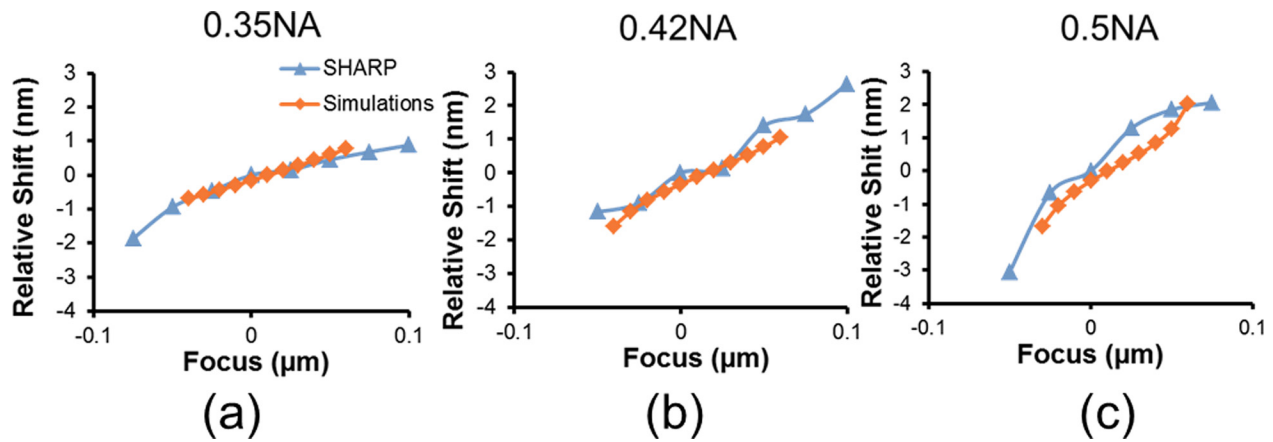


FIG. 13. (Color online) Comparison of relative pattern shift data from experiments on the SHARP with rigorous 3D mask simulations in SLitho for EUV (Synopsys) for a 36 nm pitch target grating and 180 nm pitch reference grating through NA.

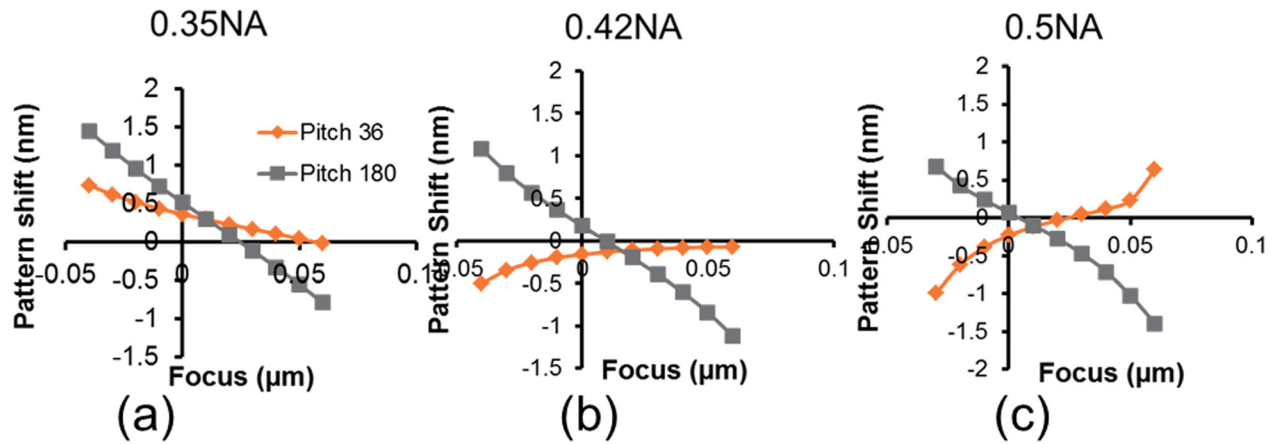


FIG. 14. (Color online) Simulation data showing individual contributions to pattern shift through focus of 36 and 180 nm horizontal pitch through NA using annular illumination (sigma setting 0.2/0.9).

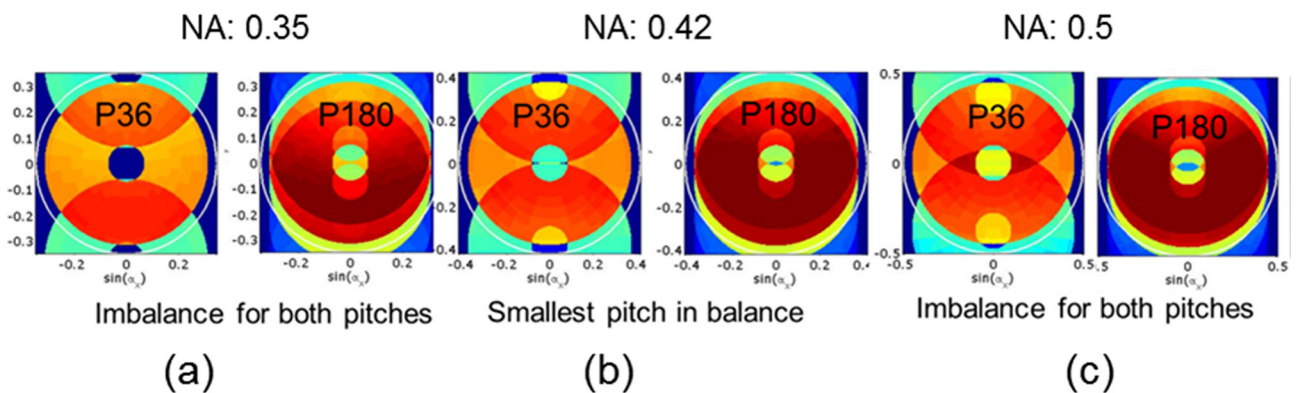


FIG. 15. (Color online) Pupil maps showing intensity of diffracted orders for 36 and 180 nm pitch horizontal gratings for the 0.2/0.9 sigma annular illuminator at NA 0.35, 0.42, and 0.50.

still present in the P180 pupil map. As a result, the relative shifts at 0.35 NA (imbalance in both) are smaller compared to 0.42 NA (imbalance in P180 only). At 0.5 NA, while P180 still shows imbalance, the orientation of the imbalance for

P36 is reversed with the top half of the pupil having more intensity than the bottom half. This results in opposite slopes in the pattern shift curves for P36 and P180, resulting in a very large relative error.

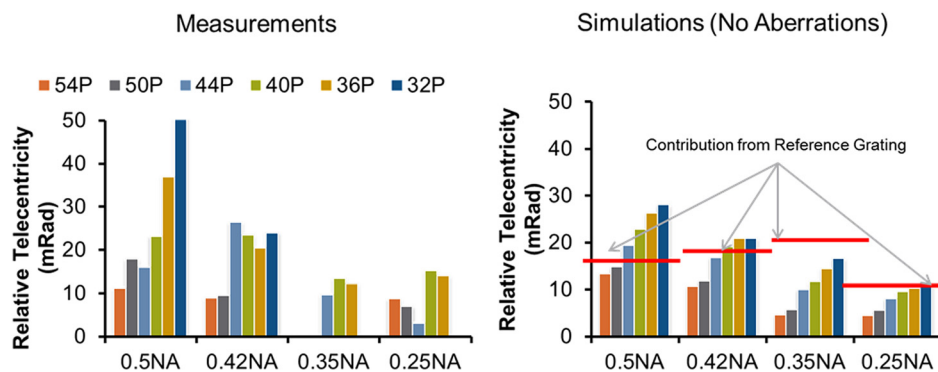


Fig. 16. (Color online) Comparison of measured and simulated relative telecentricity errors for a range of pitches through NA using annular illumination (sigma setting 0.2/0.9).

Figure 16 compares the measured and simulated data across different NA's and pitches. There is good qualitative agreement between the two sets of data. The differences between the measured and simulated curves can possibly be explained by the presence of SHARP tool imaging artifacts in the measured data. Such imaging artifacts include presence of aberrations in the zone plates, nonuniformity of the illumination on the mask, etc. Both of these artifacts, especially coma and trefoil aberrations, can exhibit behaviors similar to telecentricity-dependence, with pattern shifts through focus. Illumination nonuniformity can also mimic the imbalance seen in the pupil maps, leading to telecentricity-like effects. Both of these imaging artifacts need to be deconvolved from the measured data to better match them to simulations.

#### IV. SUMMARY AND CONCLUSIONS

Nontelecentric illumination in EUV lithography leads to a variety of 3D mask effects such as shadow bias, pattern shifts due to wafer focus error and reticle nonflatness. Mask multilayer reflectivity apodization in combination with the nontelecentric illumination results in wafer focus error induced pattern shifts, referred to as telecentricity errors. The larger the NA, the larger the telecentricity errors become. Hence, these errors are of particular importance at high NA EUV patterning where the overlay budgets are likely to be very tight. It is anticipated that telecentricity errors will become a major part of the overlay budget for future technology nodes.

Tuning the multilayer period of a EUV mask can alter the reflectivity apodization curve, changing the pattern shift behavior. Pattern shifts for a select range of pitches can be minimized by tuning the multilayer period of the mask stack. We have demonstrated the first experimental measurement of these focus induced pattern shifts in high NA EUV systems using SHARP mask inspection tool at LBNL. The imaging conditions on the SHARP mimic production EUV scanners. Using a tuned multilayer blank, relative pattern shifts were measured using specially designed test structures at 0.25, 0.35, 0.42, and 0.5 NA. The multilayer blank was tuned for critical pitch imaging at 0.42 NA. These relative

shifts were measured for a range of pitches from 36 to 54 nm. It was observed that the range of pattern shifts increases with NA. The measured data were compared to simulations and showed excellent agreement with simulations. The observed pattern shift trends were modeled using imbalances in the pupil maps. At 0.42 NA for 36-nm pitch, the pupil map showed almost perfect balance, thereby showing that the mask stack is tuned for  $\sim$ 36-nm pitch printing. The larger pitch structures exhibit the largest telecentricity errors across NA. For most lithographic applications, the critical structures from an overlay budget viewpoint are lines/spaces at the resolution limit while other structures at larger pitches have more relaxed overlay specifications.

#### ACKNOWLEDGMENTS

Measurements performed on the SHARP EUV microscope were funded by SEMATECH and conducted by the Center for X-Ray Optics at the Lawrence Berkeley National Laboratory Advanced Light Source synchrotron radiation facility. The Advanced Light Source is supported by the Director, Office of Science, Office of Basic Energy Sciences, of the U.S. Department of Energy under Contract No. DE-AC02-05CH11231.

<sup>1</sup>W. Kaiser, SEMATECH Litho-Forum, Vancouver, 2012.

<sup>2</sup>R. Peeters *et al.*, *Proc. SPIE* **8679**, 86791F (2013).

<sup>3</sup>P. A. Kearney, C. E. Moore, S. I. Tan, S. P. Vernon, and R. A. Levesque, *J. Vac. Sci. Technol.*, **B** **15**, 2452 (1997).

<sup>4</sup>S. Bajt, J. B. Alameda, T. W. Barbee, Jr., W. M. Clift, J. A. Folta, B. Kaufmann, and E. A. Spiller, *Opt. Eng.* **41**, 1797 (2002).

<sup>5</sup>S. Yulin, "Multilayer interference coatings for EUVL," in *Extreme Ultraviolet Lithography*, edited by B. Wu and A. Kumar (McGraw Hill, New York, 2009).

<sup>6</sup>V. Philipsen, E. Hendrickx, R. Jonckheere, G. Vandenberghe, N. Davydova, T. Fliervoet, and J. T. Neumann, "Impact of mask stack on high-NA EUV imaging," *International Symposium on Extreme Ultraviolet Lithography*, Brussels, 2012.

<sup>7</sup>J. T. Neumann, P. Graupner, W. Kaiser, R. Garreis, and B. Geh, *Proc. SPIE* **8522**, 852211 (2012).

<sup>8</sup>S. Raghunathan, G. McIntyre, G. Fenger, and O. Wood, *Proc. SPIE* **8679**, 867918 (2013).

<sup>9</sup>V. Philipsen, E. Hendricks, R. Jonckheere, N. Davydova, T. Fliervoet, and J. T. Neumann, *Proc. SPIE* **8886**, 88860B (2013).

<sup>10</sup>K. A. Goldberg *et al.*, *Proc. SPIE* **9048**, 90480Y (2014).